Anisole disproportionation on HZSM-5: The key role of Si/Al ratio on auto-inhibition effect

N. Pichot, J.W. Hounfodji, H. El Siblani, M. Badawi, Valentin Valtchev, S. Mintova, J.-P. Gilson, A. Dufour, L. Pinard

Anisole disproportionation on HZSM-5: the key role of Si/Al ratio on auto-inhibition effect

N. Pichot[a,b,d], J.W. Hounfodji[c], H. El Siblani[d], M. Badawi[e], V. Valtchev[d], S. Mintova[d], J-P. Gilson[d], A. Dufour[b], L. Pinard[d]

[a]Institut de Chimie des Milieux et Matériaux de Poitiers (IC2MP, UMR 7285, Université de Poitiers, France)

[b]Laboratoire Réactions et Génie des Procédés (LRGP, UMR 7274, Université de Lorraine, France)

[c]Laboratoire de Chimie-Physique, Matériaux et Modélisation Moléculaire (LCP3M, Université d'Abomey-Calavi, Bénin)

[d]Laboratoire de Catalyse et Spectrochimie (LCS, UMR 6506, ENSICaen, France)

[e]Laboratoire Lorrain de Chimie Moléculaire (L2CM, UMR 7053, Université de Lorraine, France)

Keywords

ZSM-5; DFT ; adsorption energy, aluminium siting

Abstract

The conversion of anisole has been studied at 773 K on HZSM-5 zeolites with nine Si/Al ratios ranging from 9 to 201. The influence of the distribution of Brønsted Acid Sites on catalytic activity and reaction products selectivity has been studied experimentally. The adsorption energies for reactant and products on isolated and paired aluminium have been modelled by DFT. The Si/Al ratio does not affect any selectivity. Higher concentration of Brønsted acid sites leads to higher activity from Si/Al = 201 to 29. The shift from mostly isolated to increasingly paired Al strongly inhibits the conversion and initial activity. This is attributed to product desorption becoming the limiting step in the Sabatier volcano plot. This finding is consistent with the significant increase in adsorption energies between isolated and paired sites. When the adsorption energy of gaseous anisole becomes similar to that of its products, an auto-inhibition effect takes place as already known for liquid-phase processes.

Introduction

Catalytic conversion of hydrocarbons on zeolites takes place in major oil refining processes. Heavy products, often referred to as coke, are often formed and their retention leads to deactivation by poisoning acid sites and/or blocking pores [1–6].

The catalytic conversion of biomass-derived oxygenated molecules is becoming an important route to produce green aromatics[7–10]. With these polar reactants, the deactivation can also result from the poisoning of acid sites by reaction products (auto-inhibition)[11–13]. For example, in the Friedel-Craft acetylation of anisole, the formation of small (and even minimal) amounts of polyacylated species inhibits the catalyst activity due to the strong adsorption of these products on acid sites [12,13]. Such inhibition from polar molecules is not exclusive to liquid phase reactions, but can also occur in the gas phase. Hydrocarbon cracking on HY zeolite at 623 K has shown that the addition of phenol increases the deactivation of the catalyst, due to its strong adsorption (even at high temperatures) on acidic sites [14–16]. Hence, adsorption competition between hydrocarbons and phenol governs catalyst activity. Recently, for the disproportionation of anisole on HZSM-5 at 673 K, we have shown that catalyst deactivation results in part from the inhibitory effect of the reaction products [17]. The molecules trapped in the zeolite micropores are polymethyl-phenols, and their retention is due to strong adsorption on the acid sites, as confirmed by DFT calculations.

The effects of competitive adsorption between reactants and products depend on the polarity and polarizability of the zeolite, as suggested by Derouane et al. [13]. Indeed, it was shown that during acetylation of anisole on BEA zeolite with low Al content, the initial reaction rate is proportional to the Al content, whereas the rate decreases at high Al content. This suggests that the Si/Al ratio plays a key role in the competitive adsorption effects between reactants and products, and that the inhibitory effect is mitigated on zeolite with low aluminium content [13]. The key role of the Si/Al ratio on the auto-inhibition effect seems well established for liquid phase reactions. For gas phase, DFT investigations have shown that the adsorption selectivity can be strongly tuned upon variation of the Si/Al ratio [18,19]. Does this auto-inhibition effect apply for gas-phase anisole disproportionation? Anisole is an interesting surrogate molecule to understand the catalytic conversion of methoxy-phenols produced by lignin pyrolysis [20].

The aim of this study is to investigate the impact of ZSM-5 zeolite acidity on gas-phase anisole transformation using nine commercial zeolites with Si/Al ratios ranging from 9 to 201, with particular interest on activity, product selectivity in the initial stage of the reaction, *i.e.,* on coke-free catalysts, as well as describing the interactions between oxygenates and Brønsted acid sites.

Experimental

Catalysts: ZSM-5 zeolites were sourced from Alsi-Penta (Si/Al = 12 & 24 - SM-27, SM-55), Mizusawa (Si/Al = 50 – SILTON^{TM} series), Tosoh (Si/Al = 9 & 12 – HSZ-822HOA & HSZ-820NHA), and Zeolyst (Si/Al = 29, 43, 75 & 201 – CBV5524G, CBV8014, CBV1502 & CBV28014). Some were in NH_4^+ form, therefore calcination was performed to convert to the protonic form: under N_2 (P_{atm}, 100 mL/min) at 373 K for an hour (5 K/min from room temperature) for drying, then under air (P_{atm}, 100 mL/min) at 823 K for 6 hours (10 K/min). The catalysts are referred to as follows: the capital letters A, M, T and Z for the supplier (respectively Alsi-penta, Mizusawa, Tosoh and Zeolyst), and the number for the Si/Al ratio. An asterisk is added when the catalyst contains a large amount of extra-framework aluminium species.

Characterizations: Nitrogen sorption measurements were carried out at 77 K and between 0 and 100 kPa on the zeolite with a *Micromeritics 3Flex* apparatus. The fresh samples were degassed at 623 K for 15 h. The micropore volume (V_{micro}) was calculated from the t-plot curve using the Harkins-Jura method and a thickness range between 4.5 and 5.8 Å. Total porous volume was calculated with a single point adsorption method at around $P/P^0 = 0.988$.

Solid state ^{29}Si MAS (Magic Angle Spinning) NMR spectra were performed on a Bruker Avance 400 III HD spectrometer at resonance frequency of 79.53 MHz, with a 7 mm NMR probe. The spectra were obtained using a 6µs single pulse at a spinning speed of 6 kHz, with a recycle delay of 20s. The ^{29}Si chemical shifts were referenced to tetramethylsilane (TMS) at 0 ppm.

^{27}Al MAS NMR experiments were carried out on a Bruker AVII 500 spectrometer (v27Al = 130.3 MHz). A 3.2 mm MAS NMR probe (Bruker) was used, and the MAS frequency was 5 kHz. The ^{27}Al chemical shifts were referenced to $Al(NO_3)_3$ at 0 ppm.

Catalysts Crystal particle sizes were assessed by laser diffraction (Particle size analyser – MT3000II).

Pyridine adsorption (423 K) monitored by infrared (IR) spectroscopy (*Nicolet Magna FTIR iS50* spectrometer) was used to investigate the acidity [21,22]. Samples were first pressed into thin wafers and activated *in-situ* in the IR cell at 623 K for 15 h. The interaction between pyridine and the acid sites of zeolites produces some characteristic bands for pyridine adsorbed on Brønsted and Lewis acid sites in the 1300-1700 cm^{-1} region: pyridinium ions (1490, 1545, 1640 cm^{-1}) and coordinated pyridine (1455, 1490, 1600-1630 cm^{-1}). Their concentration was calculated using the Beer-Lambert-Bouguer's law: $C = \frac{A}{\varepsilon} \times \frac{S}{m} \times 1000$, where C is the acid sites concentration (µmol.g^{-1}), A the band's area (absorption.cm^{-1}), S the wafer's surface (2 cm^2), m the mass of the wafer (mg), and ε the molar extinction coefficient (cm.µmol^{-1}).

Molar extinction coefficients were previously determined to be respectively 1.13 cm.µmol^{-1} and 1.28 cm.µmol^{-1} for Brønsted and Lewis acid sites [22].

Catalytic tests: The catalytic tests were carried out in a continuous down-flow tubular fixed bed reactor. Before test, catalysts were shaped into particles of 0.2 < ø < 0.4 mm diameter (pellets formed under 500 kg, crushed and sieved). The catalyst pre-treatment began by heating to 373 K (1 K.min^{-1} from ambient), with a 1 h plateau, to avoid any steaming damage from adsorbed water. Further heating (1 K.min^{-1}) to 673 K followed with a 1 h plateau at the final temperature. Liquid Anisole was then injected (0.01 mL.min^{-1}) with a *Metrohm 725 Dosimat* and instantaneously vaporized at the reactor inlet. The operating conditions were as follows: $P_{anisole}$ = 0.048 atm, N_2 flowrate (STP)= 100 mL.min $^{-1}$, T = 673 K. All lines after the reactor were heated at 623 K to avoid condensation of reactant and products ($T_{lines} > T_{boil} + 50$).

Reaction products were injected online in a GC-FID from Scion (*456-GC, Scion5-MS column*, 30 m - 0.25 mm - 25 µm) and identified by GC-MS (GC-QTOF, *Agilent*).

Atomistic simulations: Periodic DFT calculations were performed using the VASP code [23]. PAW pseudopotentials have been used [24] with the PBE+D2 level of theory [25,26]. The plane-wave cut-off energy was set to 450 eV, following a series of convergence test. The equations of Kohn-Sham [27,28] were solved by self-consistent field (SCF) iteration until total energies were converged to within 1 x 10^{-6} eV as convergence criterion. The ionic relaxation of all the structures was carried out systematically until the force of each atom was less than 0.02 eV/A.. The integration zone of the Brillouin zone was sampled using only the (1 x 1 x 1) k-point grid.

The adsorption energies ΔE_{ads} of guest molecules in the porous matrix have been computed as follows (**eq. 1**):

$$\Delta E_{ads} = E_{(zeol-X)} - E_{(zeol)} - E_{(X)} \qquad \textbf{(eq. 1)}$$

With $E_{zeolite}$ the energy of the empty zeolite, E_X the energy of the isolated molecule, and $E_{zeolite\text{-}X}$, the energy of the relaxed zeolite with the molecule inside.

Results and discussions

Characterization of commercial zeolites: Table 1 summarizes the textural and acidic properties of the commercial H-ZSM-5 zeolites: Alsi Penta (A), Misuzawa (M), Tosoh (T) and Zeolyst (Z). On all materials, micropore volumes correspond to an MFI structure, i.e. around 0.16 cm^3.g^{-1} [29,30], and mesopore volumes are relatively low, below 0.10 cm^3.g^{-1} (**Figure 1a**). Particles are around 8 µm in diameter.

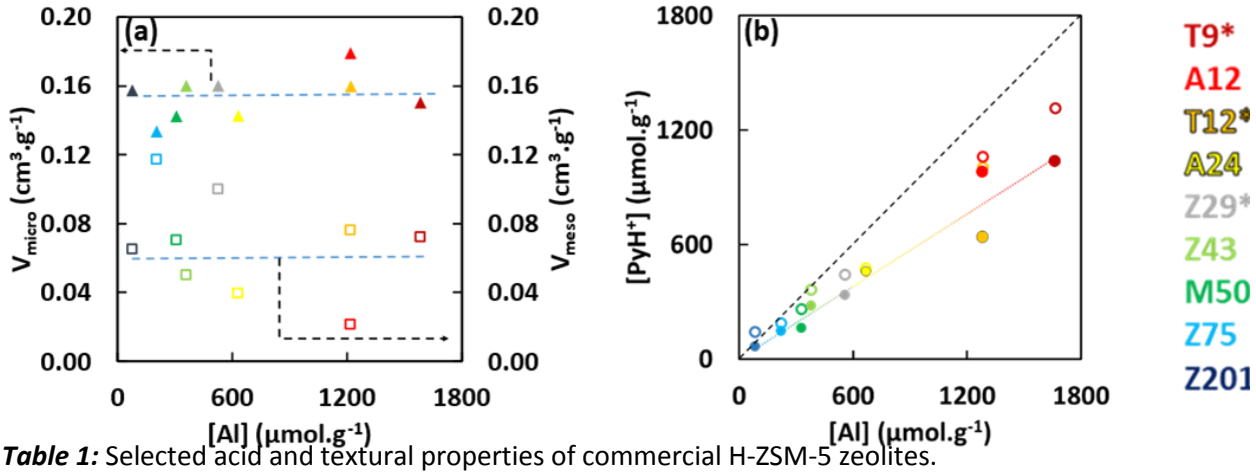

Table 1: Selected acid and textural properties of commercial H-ZSM-5 zeolites.

Catalyst¤	Supplier	Si/Al[a]	[PyH+][b]	[PyL][b]	V_{micro}[c]	V_{meso}[d]	Particle size[e]
		mol/mol	µmol.g^{-1}	µmol .g^{-1}	cm^3.g^{-1}	cm^3.g^{-1}	µm
T9*	T	9	1038	139	0.15	0.07	9.00
A12	A	12	980	41	0.18	0.02	
T12*	T	12	641	183	0.16	0.08	7.59
A24	A	24	463	7	0.14	0.04	
Z29*	Z	29	338	53	0.16	0.10	
Z43	Z	43	281	49	0.16	0.05	
M50*	M	50	164	50	0.14	0.07	7.66
Z75	Z	75	148	21	0.13	0.12	
Z201	Z	201	67	38	0.16	0.07	

¤Catalysts are labelled with a letter (supplier) and a number (Si/Al ratio)
[a] ICP analysis, [b] concentration of pyridine adsorbed on Brønsted (PyH^+) and Lewis (PyL) acid sites, respectively, after evacuation at 423 K; [c] microporous volume calculated using the t-plot method ; [d] mesoporous volume $=V_{total}-V_{micro}$ (V_{total} : volume adsorbed at $P/P_0=0.98$); [e] particle sizes obtained with particle size analyser - SYNC[32]; *Presence of large amount of EFAl species, seen either with IR or (^{27}Al) MAS NMR spectrometry

Nitrogen physisorption isotherms are provided as **Figure S1**. They show type I isotherms for all catalysts but Z29, T9* and T12. These show an H3 or H4 type hysteresis; they are nanoparticle agglomerates, as opposed to others, which are micron sized catalysts[31]. This is corroborated in **Figure S2** by the SEM analysis of T9*, T12, Z43 and M50. T9* and T12 clearly show the micron-sized agglomerates of nano-sized crystals, while Z43 shows micron-sized crystal intergrowths and M50 shows very well-defined micron-sized crystals. This results in shorter diffusion pathways for reactants and products in T9* and T12, compared to Z43 and M50.

Figure 1: **(a)** Micro and mesoporous volumes of the selected zeolites; **(b)** Comparison between measured acidity (µmol.g^{-1}) and measured Al (µmol.g^{-1}) content in the selected zeolites. Full symbols: measured BAS; Open symbols: sum of measured LAS and BAS. Black dotted line: [Al] = [PyH^{+}].

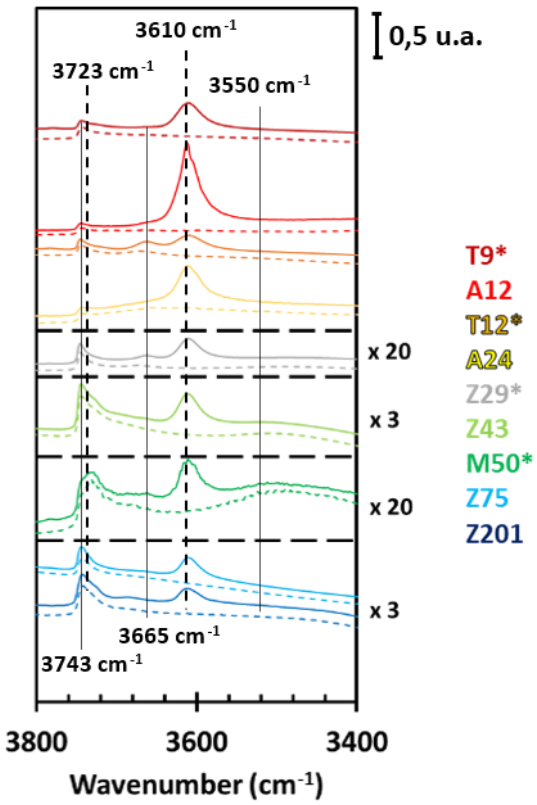

Figure 2: FTIR spectra in the hydroxyl group stretching region before (full line) and after (dotted lines) pyridine adsorption at 423 K.

The concentration of Brønsted acid sites (BAS) probed by IR monitoring of adsorbed pyridine ranges from 67 to 1038 µmol.g^{-1} and, except for Tosoh zeolites, is proportional to the aluminium content measured by ICP (**Figure 1b**), suggesting that most aluminium atoms are in the zeolite framework. As a result, the concentration of Lewis acid sites (LAS) is low, below 50 µmol.g^{-1} for most of the catalysts. In contrast, on T9* and T12*, LAS concentrations are high, 139 and 183 µmol.g^{-1}, respectively, suggesting that these materials may be partially dealuminated during the 673 K calcination.

Figure 2 compares the hydroxyl band intensities of the different zeolites. The bands at 3743 cm^{-1} with a shoulder at 3723 cm^{-1} are attributed to external and internal silanol, respectively. A large amount of internal silanol on M50* results in the appearance of a broad band at 3550 cm^{-1} ascribed to hydroxyl nests [33]. The silanol groups present on high aluminium content zeolites retain pyridine

at 423 K, whilst on zeolites with a lower Al content, the silanol groups are not acidic enough to retain pyridine at 423 K.

The band at 3610 cm^{-1} corresponds to bridged hydroxyls (BAS) and increases with decreasing Si/Al ratio. The band at 3665 cm^{-1} is assigned to extra-framework aluminium species (EFAl). The presence of hydroxylated EFAl species is limited on all commercial zeolites, except T12*; they can limit pyridine accessibility to BAS. On T9*, all the BAS are accessible to pyridine despite a large amount of non-hydroxylated EFAl species, suggesting that the latter are located outside the zeolite crystal.

Aluminium speciation in H-ZSM-5 catalysts is investigated by single pulse 27Al MAS NMR experiments on hydrated samples. The relative amounts of tetrahedrally coordinated framework Al at bridging acid sites (BASs) versus non-framework, octahedrally coordinated Al (Al(VI)) are obtained from the integrated areas of the ~55 and 0 ppm peaks, respectively (**Figure 3**).

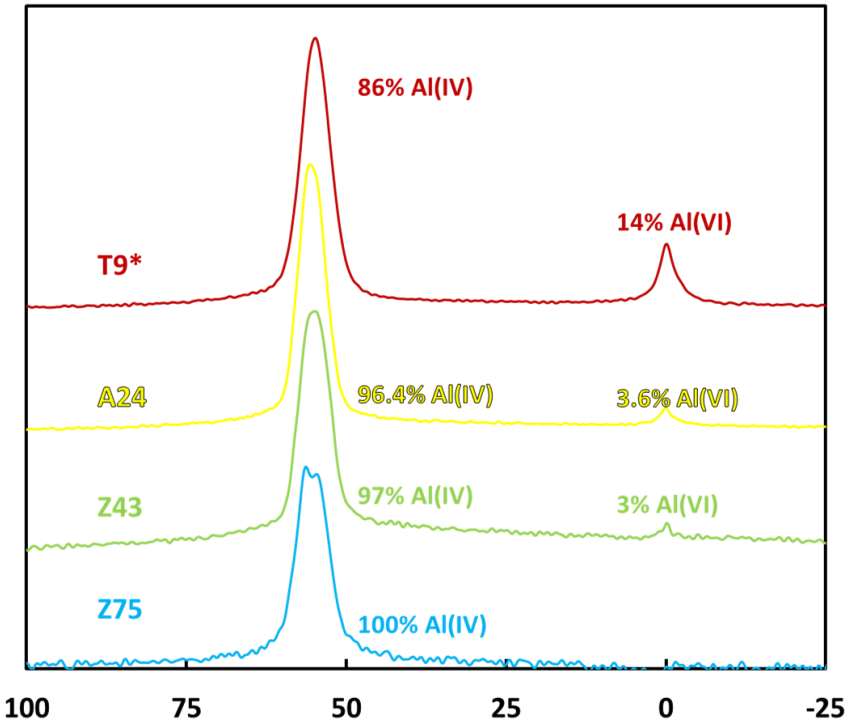

Figure 3 ^{27}Al MAS NMR spectra of **T9***, **A24**, **Z43** and **Z75** samples

Only the T9* catalyst presents a high amount of extra framework Al (14%), while A24, Z43 and Z75 present 3.6, 3 and 0% of those species, respectively. These values are in accordance with the IR spectra in **Figure 2**.

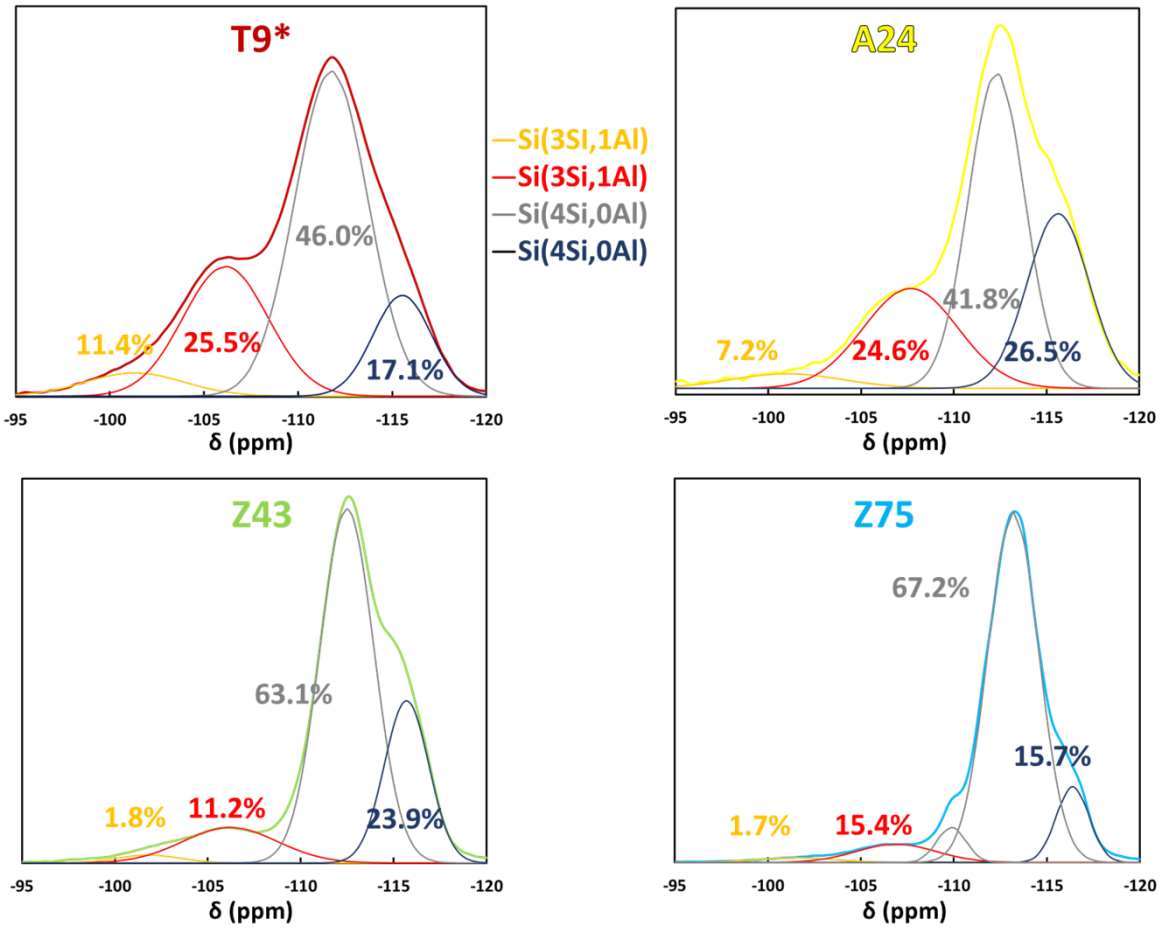

Figure 4: ^{29}Si NMR spectra for catalysts **T9***, **A24**, **Z43** and **Z75** in the Al substitution region[34,35].

Figure 4 compares the ^{29}Si NMR spectra of catalysts T9*, A24, Z43 and Z75 showing the distribution of Al species around Si atoms in the MFI structure. Peaks from 110 ppm (grey and dark blue) show Si atoms with only other Si atoms in neighbouring positions (Si(-O-Si)4). Red bands around 105 to 107 ppm show either Si atoms with an adjacent Al or a terminal silanol. Finally, yellow bands around 100 ppm show Si atoms with an Al in a neighbouring position. In all four spectra there is no noticeable peak around 95 ppm, indicating the absence of two Al atoms in an NNN (Next Nearest Neighbour, i.e. separated by one Si atom) position: the closest Al atoms could be to each other is in the NNNN (Next Next Nearest Neighbour, i.e. separated by two Si atoms) position, within the same 10 Membered-Ring (**10 MR**) [36]. This observation underlines the structural limitations of Al clustering within the zeolite framework. As expected, the lower the Si/Al ratio, the higher the density of Si with Al in a neighbouring position. Conversely, the higher the Si/Al ratio, the higher the number of "isolated" Si atoms. Pairing of aluminium atoms was verified by Co2+ exchange followed by IR in another work on T9* (Sold by Tosoh as an HZSM-5 Si/Al = 12.5), and produced 68% of “paired” Al [37].

Initial activity and selectivity: The conversion of anisole was studied at 673 K on the nine commercial catalysts. **Figure 5a** shows the natural logarithm of initial conversion as a function of contact time (W/F). A straight line through the origin is obtained, regardless of the Si/Al ratio. Although the anisole transformation is a bimolecular reaction, it follows an apparent first-order kinetic rate[17].

Figure 5b plots the initial catalyst activity as a function of the BAS concentration. From a Si/Al ratio of 29 upwards, the initial activity is proportional to BAS concentration, except on M50* due to EFAl blocking their access. The turnover frequency of Brønsted acid sites (**Figure 5c**) is high, on the order of 400-500 h^{-1}, but unexpectedly, increasing aluminium content is detrimental to anisole disproportionation. This is not due to pore blocking by EFAl species, as initial activity is very low on low Si/Al, EFAl-free catalysts, such as A12 (**Figure 2**). The length of the diffusion path also is not a major factor here, with T9* and T12 being nanosized crystals, with shorter diffusion paths, that should help with outward diffusion of the reactant and products, and overall, with activity.

Catalysts with higher Brønsted acidities (T9*, T12*,A12, A24*) show very low activities (**Figure 5b**). Among them, T9* and T12* exhibit somewhat higher activities than the other two. They also differentiate by their higher LAS count (**Table 1**). Assuming that, with these lower Si/Al ratios, BAS have no activity (seen for A12 and A24*, **Figure 5c**), a TOF_0 for T9* and T12*'s Lewis acid sites can be calculated, giving 61.4 h^{-1} and 100.1 h^{-1} respectively. This indicates that, for these low Si/Al ratios catalysts, LAS display some activity, albeit 8 to 10 times inferior to the one shown by higher Si/Al ratios BAS. Lewis acidity has already been shown to help guaiacol adsorption [38] on Y zeolites, and also improve catalyst stability in the context of pyrolysis vapor catalytic upgrading on HZSM-5 [39].

Terminal silanol groups have recently been shown to have some acid strength, positively correlated with Al concentration[40], and that could provide additional activity to neighbouring BAS. While this effect could be present here, **Figure 2** shows the very low acidity of silanol groups in higher Si/Al zeolites, and also their very low concentration for lower Si/Al zeolites, thus rendering their effect negligible at best in this study.

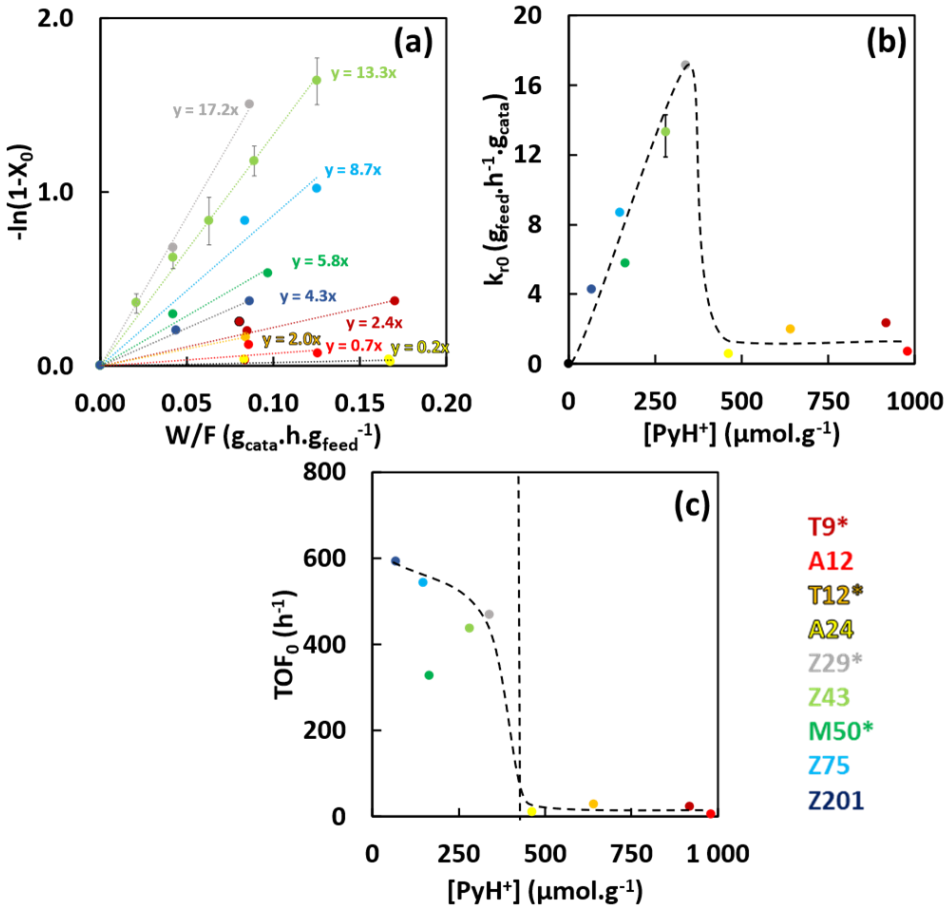

Figure 5: **(a)** Test for the first order rate equation for anisole transformation at 673 K on MFI zeolites with different Si/Al ratio **($-\ln(1-X_0) = k_{r0} \cdot \frac{W}{F}$)**; **(b)** Initial rates (k_{r0}, $g_{feed}.h^{-1}.g_{cata}^{-1}$) as a function of catalyst initial acidity; **(c)** Initial Turnover Frequency (h^{-1}) as a function of initial acidity.

Anisole (An) transformation produces phenol (Ph), *o-, m-, p*-methylanisols (MA), *o-, m-, p*-cresols (Cr), 2,4-, 2,5-xylenols (Xol). The deoxygenated aromatics yield is low, and the quasi absence of methane production suggests that the cleavage of aryl ethers does not occur. **Figure 6** shows the yields of initial products as a function of initial anisole conversion. Phenol and methylanisoles are primary products, cresol a secondary product appearing at low conversion (< 5%) and xylenols are tertiary products appearing at conversion above 20% [17]. Si/Al molar ratio has no impact on product selectivity, but only on the initial activity.

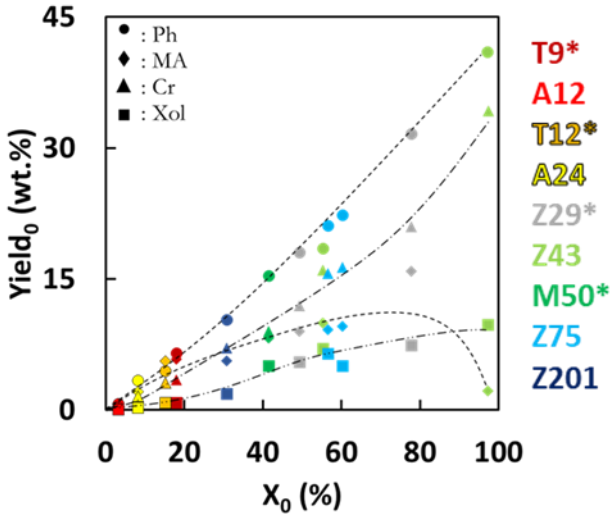

Figure 6: Initial yields for phenol, methylanisoles, cresols and xylenols *vs* initial conversion.

The low activity of the Al-rich zeolites (Si/Al ≤ 24) could be related to Al distribution in the framework. Indeed, the ^{29}Si NMR results showed that on the aluminium-poor zeolite, Al atoms are isolated, while on the aluminium-rich zeolite, in addition to the isolated Al, two Al in the NNNN (Next Next Nearest Neighbour) position are possible. To investigate the effect of aluminium distribution on catalyst activity, the adsorption energies of anisole and disproportionation products on isolated Al and on two Al in NNNN, NNN and opposite positions were modelled.

Computed adsorption energies of phenolic compounds: Among the 12 distinct T sites in H-ZSM-5 zeolite, Al11 (equivalent to Al5) and Al12 (equivalent to Al6) are identified as the most representative isolated sites [41]. When associated with a next nearest neighbour (NNN configuration), Al3 (equivalent to Al9) is selected for Al11 and Al7 (equivalent to Al1) for Al12 [42,43]. For the NNNN and opposite configurations, the pairs Al8 & Al5 and Al8 & Al2 have been selected. **Table 2** compares the adsorption energies, ΔE_{ads} on these Al atoms for selected molecules (reactant and products). All the adsorption energies are negative, indicating their exothermic nature. Moreover, a consistent difference of approximately 50 kJ.mol^{-1} is observed between the isolated and paired sites.

Table 2: Adsorption energies for oxygenated compounds on paired and unpaired Al sites on 10 MR MFI zeolites

	ΔE_{ads} (kJ.mol^{-1})					
	Al11	Al12	Al8 & Al2 (opposite)	Al3 & Al11 (NNN)	Al7 & Al12 (NNN)	Al8 & Al5 (NNNN)
Anisole	**-110.0**	**-133.7**	**-141.9**	**-155.3**	**-170.2**	**-179.1**
o-Methylanisole	-108.8	-104.1	-143.3	-155.2	-146.0	-161.2
m-Methylanisole	-137.0	-145.1	-150.9	-166.1	-153.3	-183.5
p-Methylanisole	-139.1	-129.0	-164.0	-174.8	-160.5	-173.0
Phenol	-82.1	-100.6	-130.2	-152.3	-128.5	-168.0
o-Cresol	-103.0	-114.6	-134.8	-131.7	-138.3	-150.0
m-Cresol	-90.2	-116.1	-132.3	-124.4	-130.2	-153.9
p-Cresol	-110.5	-124.9	-152.4	-179.2	-153.3	-177.1
2,4-Xylenol	-96.0	-123.7	-156.2	-144.7	-161.3	-180.2
2,5-Xylenol	-110.9	-123.0	-160.5	-178.5	-143.5	-186.7

Figure 7 compares the final geometry of the anisole and phenol molecules on isolated Al12, Al8 & Al2 in opposite position and Al8 & Al5 in NNNN positions. Figures showing the final geometries of multiple molecules (reactant and products) are also given in the Supporting Information. (**Figures S3 to S12**).

Anisole adsorbs by forming a hydrogen bond between its oxygen and the Brønsted acid site on isolated Al12 and one between its oxygen and each BAS for Al in the NNNN position. In the case of phenol (and by extension cresol and xylenol), in addition to the oxygen bond of the molecule, a second bond appears on the isolated Al12. The alcohol proton has formed a hydrogen bond with an oxygen atom in the zeolite. For the NNNN sites, phenol (and by extension Cr and Xol) adsorbs only with its oxygen, which forms a hydrogen bond with each BAS. For isolated Al, the adsorption energies of ethers (anisole, MA) were higher than those of phenols, even with the second H-bond (**Table 2**). This is still the case for paired (NNN, NNNN, and opposite) sites, although the energy difference is much smaller. For the opposite configuration, due to the distance between the two aluminium atoms, it is not possible to form hydrogen bonds with both BAS simultaneously, reducing the adsorption energies by about 20 to 30 kJ.mol^{-1} (**Table 2**).

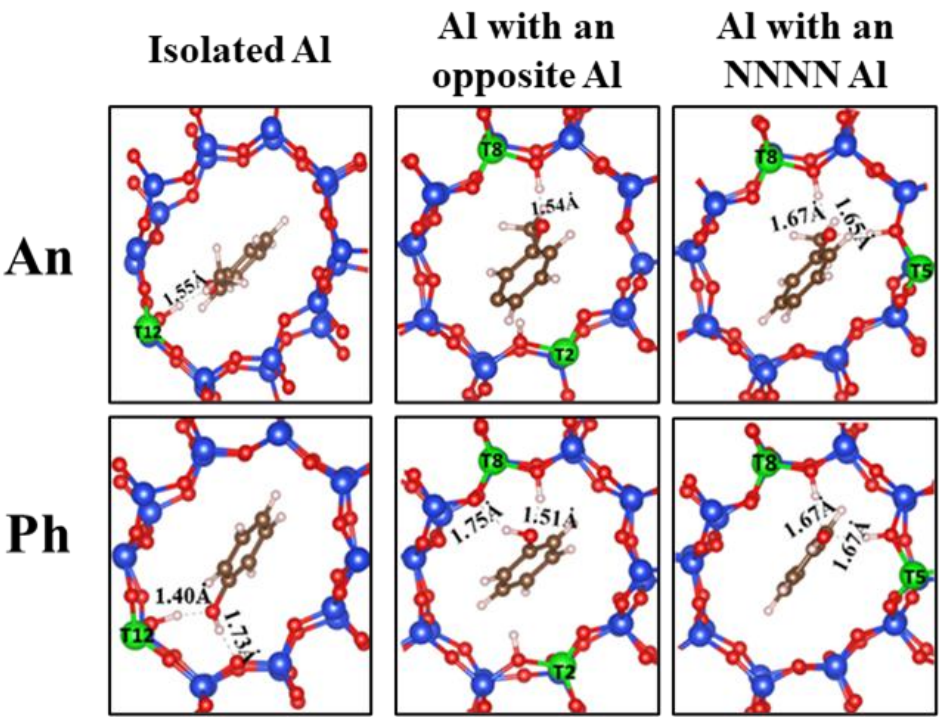

Figure 7: Final geometries of anisole and phenol adsorbed on isolated aluminium, as well as aluminium with another (NNNN and opposite) aluminium in the 10 MR.

The adsorption energy (E_{ads}) is always lower when the aluminium is isolated, regardless of the oxygenated molecules (**Table 2**). If a second aluminium atom is present on the 10 MR, E_{ads} increases significantly, even if it is in the opposite position. Irrespective of the oxygenated molecules, Eads decreases by 30-40 kJ.mol^{-1} when a second aluminium atom is in the NNN position in the 10-MR, and by a further 20-30 kJ.mol^{-1} when it is in the NNNN position. Therefore, the stronger adsorption site for oxygenated compounds is two aluminium atoms in the Next Next Nearest Neighbour position. According to the Sabatier principle, the high adsorption energy of the oxygenated molecules could create an auto-inhibitory effect where the desorption of phenolic molecules is the rate-limiting step for anisole conversion. The key role of the Si/Al ratio on the auto-inhibition effect seems well established for gas-phase reactions involving oxygenated compounds. The present results also pave the way for potential advances in the design of more efficient and selective catalysts for gas-phase conversion processes of phenolic compounds.

Conclusion

The conversion of anisole at 673 K under atmospheric pressure and on nine HZSM-5 with Si/Al ratios ranging from 9 to 201 has been carried out. Catalyst initial activity and product selectivity were the main experimental focus, and product adsorption energies computed by DFT.

Si/Al ratio, while greatly affecting initial conversion, does not affect product selectivity, which is only correlated to conversion and zeolite structure (confinement effect). This influence on conversion, therefore activity, is explained in large part by differences in anisole adsorption energies between isolated and paired active sites, and the reduced gap between adsorption energies of anisole and phenolics on paired sites ($27.9 < \Delta_{\mathrm{An-Ph}}^{Isolated\ Al} < 33.1$ kJ.mol^{-1} vs $11.1 < \Delta_{\mathrm{An-Ph}}^{Paired\ Al} < 11.7$ kJ.mol^{-1}). This smaller gap on paired sites prevents anisole from displacing other adsorbates. This is a typical illustration of the Sabatier principle, where a decrease in Si/Al ratio leads to an auto-inhibition effect by making phenolics desorption the rate-limiting step of the process. Even the shorter diffusion pathways of the nano-sized zeolites in the study do not prevent or mitigate it. This auto-inhibition effect, previously evidenced for liquid-phase (Derouane et al.), is highlighted here for gas-phase anisole disproportionation.

Further studies could focus on the effect of Al distribution and density on deactivation, as well as coke composition and retention in the zeolite. Moreover, well-engineered (identical crystal size, well-controlled “defect” nature and quantity, …) ZSM-5 with varying Si/Al ratios could lead to the design of even more optimal catalysts fitted for regeneration.

Acknowledgements

Nathan Pichot would like to thank the French Agence Nationale de la Recherche (ANR) and Région Nouvelle-Aquitaine for their financial support, through the PYCASSO and SHAPING projects. Similarly, Ludovic Pinard thanks the Région Normandie for their financial support, through the Bio/DNH project.

The authors thank the Xylofutur label for their support.

The authors acknowledge the precious work and help of Jean-Dominique Comparot (IC2MP, Poitiers) on Pyridine-FTIR and N_2-Physisorption analyses.

Jean Wilfried Hounfodji and Michael Badawi acknowledge the computer and storage resources provided by GENCI at TGCC thanks to the grant 2023-A0140810433 on the supercomputer Joliot Curie’s ROME.

Declaration of competing interests

The authors declare having no known competing financial or personal interests that could have influenced the work and results discussed in the present paper.

Authors contribution credit

Nathan Pichot: Experimental work, data exploitation, first draft, review, editing.

Jean Wilfried Hounfodji, Michael Badawi: DFT Calculations, review, editing.

Hussein El Siblani: ^{29}Si NMR measurement and exploitation, review, editing.

Svetlana Mintova, Valentin Valtchev: Review, editing.

Jean-Pierre Gilson: Discussion, review, editing.

Anthony Dufour: Supervision, funding, review, and editing.

Ludovic Pinard: Supervision, design of experimental work, data exploitation, funding, review, and editing

References

[1] M. Guisnet, F.R. Ribeiro, eds., Deactivation and regeneration of zeolite catalysts, Imperial College Press ; Distributed by World Scientific, London : Singapore, 2011.

[2] M. Guisnet, P. Magnoux, Organic chemistry of coke formation, Applied Catalysis A: General. 212 (2001) 83–96. https://doi.org/10.1016/S0926-860X(00)00845-0.

[3] M. Guisnet, L. Costa, F.R. Ribeiro, Prevention of zeolite deactivation by coking, Journal of Molecular Catalysis A: Chemical. 305 (2009) 69–83. https://doi.org/10.1016/j.molcata.2008.11.012.

[4] J.R. Rostrup-Nielsen, Industrial relevance of coking, Catalysis Today. 37 (1997) 225–232. https://doi.org/10.1016/S0920-5861(97)00016-3.

[5] G.A. Fuentes, C.H. Bartholomew, Catalyst Deactivation 1997, Elsevier, 1997.

[6] M. Argyle, C. Bartholomew, Heterogeneous Catalyst Deactivation and Regeneration: A Review, Catalysts. 5 (2015) 145–269. https://doi.org/10.3390/catal5010145.

[7] L.Y. Jia, M. Raad, S. Hamieh, J. Toufaily, T. Hamieh, M. Bettahar, G. Mauviel, M. Tarrighi, L. Pinard, A. Dufour, Catalytic fast pyrolysis of biomass : superior selectivity of hierarchical zeolite to aromatics, Green Chem. 19 (2017) 5442–5459. https://doi.org/10.1039/C7GC02309J.

[8] J. Liang, G. Shan, Y. Sun, Catalytic fast pyrolysis of lignocellulosic biomass: Critical role of zeolite catalysts, Renewable and Sustainable Energy Reviews. 139 (2021) 110707. https://doi.org/10.1016/j.rser.2021.110707.

[9] S. Wan, Y. Wang, A review on ex situ catalytic fast pyrolysis of biomass, Front. Chem. Sci. Eng. 8 (2014) 280–294. https://doi.org/10.1007/s11705-014-1436-8.

[10] A.J. Foster, J. Jae, Y.-T. Cheng, G.W. Huber, R.F. Lobo, Optimizing the aromatic yield and distribution from catalytic fast pyrolysis of biomass over ZSM-5, Applied Catalysis A: General. 423–424 (2012) 154–161. https://doi.org/10.1016/j.apcata.2012.02.030.

[11] D. Rohan, C. Canaff, E. Fromentin, M. Guisnet, Acetylation of anisole by acetic anhydride over a HBEA zeolite—Origin of deactivation of the catalyst, Journal of Catalysis. 177 (1998) 296–305. https://doi.org/10.1006/jcat.1998.2108.

[12] E.G. Derouane, C.J. Dillon, D. Bethell, S.B. Derouane-Abd Hamid, Zeolite Catalysts as Solid Solvents in Fine Chemicals Synthesis 1. Catalyst Deactivation in the Friedel–Crafts Acetylation of Anisole, (n.d.).

[13] E.G. Derouane, G. Crehan, C.J. Dillon, D. Bethell, H. He, S.B. Derouane-Abd Hamid, Zeolite Catalysts as Solid Solvents in Fine Chemicals Synthesis, Journal of Catalysis. 194 (2000) 410–423. https://doi.org/10.1006/jcat.2000.2933.

[14] I. Graça, J.-D. Comparot, S. Laforge, P. Magnoux, J.M. Lopes, M.F. Ribeiro, F.R. Ribeiro, Effect of phenol addition on the performances of H–Y zeolite during methylcyclohexane transformation, Applied Catalysis A: General. 353 (2009) 123–129. https://doi.org/10.1016/j.apcata.2008.10.032.

[15] I. Graça, A. Fernandes, J.M. Lopes, M.F. Ribeiro, S. Laforge, P. Magnoux, F. Ramôa Ribeiro, Effect of phenol adsorption on HY zeolite for n-heptane cracking: Comparison with methylcyclohexane, Applied Catalysis A: General. 385 (2010) 178–189. https://doi.org/10.1016/j.apcata.2010.07.011.

[16] I. Graça, A.M. Carmo, J.M. Lopes, M.F. Ribeiro, Improving HZSM-5 resistance to phenolic compounds for the bio-oils/FCC feedstocks co-processing, Fuel. 140 (2015) 484–494. https://doi.org/10.1016/j.fuel.2014.10.002.

[17] N. Pichot, J.W. Hounfodji, M. Badawi, V. Valtchev, S. Mintova, J.-P. Gilson, A. Dufour, L. Pinard, Products and coke shape-selectivity during anisole disproportionation over HZSM-5, Applied Catalysis A: General. 665 (2023) 119352. https://doi.org/10.1016/j.apcata.2023.119352.

[18] S. Chibani, M. Chebbi, S. Lebègue, L. Cantrel, M. Badawi, Impact of the Si/Al ratio on the selective capture of iodine compounds in silver-mordenite: a periodic DFT study, Physical Chemistry Chemical Physics. 18 (2016) 25574–25581. https://doi.org/10.1039/C6CP05015H.
[19] T. Ayadi, M. Badawi, L. Cantrel, S. Lebègue, Rational approach for an optimized formulation of silver-exchanged zeolites for iodine capture from first-principles calculations, Molecular Systems Design & Engineering. 7 (2022) 422–433. https://doi.org/10.1039/D1ME00149C.
[20] X. Zhu, R.G. Mallinson, D.E. Resasco, Role of transalkylation reactions in the conversion of anisole over HZSM-5, Applied Catalysis A: General. 379 (2010) 172–181. https://doi.org/10.1016/j.apcata.2010.03.018.
[21] J. Ward, The nature of active sites on zeolites IX. Sodium hydrogen zeolite, Journal of Catalysis. 13 (1969) 364–372. https://doi.org/10.1016/0021-9517(69)90445-X.
[22] C. Miranda, J. Urresta, H. Cruchade, A. Tran, M. Benghalem, A. Astafan, P. Gaudin, T.J. Daou, A. Ramírez, Y. Pouilloux, A. Sachse, L. Pinard, Exploring the impact of zeolite porous voids in liquid phase reactions: The case of glycerol etherification by tert-butyl alcohol, Journal of Catalysis. 365 (2018) 249–260. https://doi.org/10.1016/j.jcat.2018.07.009.
[23] G. Kresse, J. Hafner, *Ab initio* molecular dynamics for liquid metals, Phys. Rev. B. 47 (1993) 558–561. https://doi.org/10.1103/PhysRevB.47.558.
[24] G. Kresse, D. Joubert, From ultrasoft pseudopotentials to the projector augmented-wave method, Physical Review B. 59 (1999) 1758–1775. https://doi.org/10.1103/PhysRevB.59.1758.
[25] J.P. Perdew, K. Burke, M. Ernzerhof, Generalized Gradient Approximation Made Simple, Phys. Rev. Lett. 77 (1996) 3865–3868. https://doi.org/10.1103/PhysRevLett.77.3865.
[26] S. Grimme, Semiempirical GGA-type density functional constructed with a long-range dispersion correction, J. Comput. Chem. 27 (2006) 1787–1799. https://doi.org/10.1002/jcc.20495.
[27] P. Hohenberg, W. Kohn, Inhomogeneous Electron Gas, Phys. Rev. 136 (1964) B864–B871. https://doi.org/10.1103/PhysRev.136.B864.
[28] W. Kohn, L.J. Sham, Self-Consistent Equations Including Exchange and Correlation Effects, Phys. Rev. 140 (1965) A1133–A1138. https://doi.org/10.1103/PhysRev.140.A1133.
[29] F.R. Ribeiro, M. Guisnet, Les zéolithes, un nanomonde au service de la catalyse, EDP Sciences, 2012.
[30] I. Batonneau-Gener, A. Sachse, Determination of the Exact Microporous Volume and BET Surface Area in Hierarchical ZSM-5, J. Phys. Chem. C. 123 (2019) 4235–4242. https://doi.org/10.1021/acs.jpcc.8b11524.
[31] K.S.W. Sing, Reporting physisorption data for gas/solid systems with special reference to the determination of surface area and porosity (Recommendations 1984), Pure and Applied Chemistry. 57 (1985) 603–619. https://doi.org/10.1351/pac198557040603.
[32] Laser Diffraction (LD): Particle Size Analyzers :: Microtrac, (n.d.). https://www.microtrac.com/products/particle-size-shape-analysis/laser-diffraction/ (accessed August 31, 2023).
[33] L. Lin, X. Zhang, N. He, J. Liu, Q. Xin, H. Guo, Operando Dual Beam FTIR Study of Hydroxyl Groups and Zn Species over Defective HZSM-5 Zeolite Supported Zinc Catalysts, Catalysts. 9 (2019) 100. https://doi.org/10.3390/catal9010100.
[34] C.J.H. Jacobsen, C. Madsen, T.V.W. Janssens, H.J. Jakobsen, J. Skibsted, Zeolites by con®ned space synthesis ± characterization of the acid sites in nanosized ZSM-5 by ammonia desorption and 27Al/29Si-MAS NMR spectroscopy, Microporous and Mesoporous Materials. (2000).
[35] D.S.A. Silva, W.N. Castelblanco, D.H. Piva, V. De Macedo, K.T.G. Carvalho, E.A. Urquieta-González, Tuning the Brønsted and Lewis acid nature in HZSM-5 zeolites by the generation of intracrystalline mesoporosity—Catalytic behavior for the acylation of anisole, Molecular Catalysis. 492 (2020) 111026. https://doi.org/10.1016/j.mcat.2020.111026.
[36] M.J. Rice, A.K. Chakraborty, A.T. Bell, Al Next Nearest Neighbor, Ring Occupation, and Proximity Statistics in ZSM-5, Journal of Catalysis. 186 (1999) 222–227. https://doi.org/10.1006/jcat.1999.2544.

[37] J. Dědeček, D. Kaucký, B. Wichterlová, O. Gonsiorová, Co 2+ ions as probes of Al distribution in the framework of zeolites . ZSM-5 study, Physical Chemistry Chemical Physics. 4 (2002) 5406–5413. https://doi.org/10.1039/B203966B.
[38] J.M. Silva, M.F. Ribeiro, I. Graça, A. Fernandes, Bio-oils/FCC co-processing: Insights into the adsorption of guaiacol on Y zeolites with distinct acidity and textural properties, Microporous and Mesoporous Materials. 323 (2021) 111170. https://doi.org/10.1016/j.micromeso.2021.111170.
[39] X. Li, X. Zhang, S. Shao, L. Dong, J. Zhang, C. Hu, Y. Cai, Catalytic upgrading of pyrolysis vapor from rape straw in a vacuum pyrolysis system over La/HZSM-5 with hierarchical structure, Bioresource Technology. 259 (2018) 191–197. https://doi.org/10.1016/j.biortech.2018.03.046.
[40] P. Bräuer, O. Situmorang, P.L. Ng, C. D'Agostino, Effect of Al content on the strength of terminal silanol species in ZSM-5 zeolite catalysts: a quantitative DRIFTS study without the use of molar extinction coefficients, Phys. Chem. Chem. Phys. 20 (2018) 4250–4262. https://doi.org/10.1039/C7CP07826A.
[41] A.J. Jones, E. Iglesia, The Strength of Brønsted Acid Sites in Microporous Aluminosilicates, ACS Catal. 5 (2015) 5741–5755. https://doi.org/10.1021/acscatal.5b01133.
[42] P. Losch, H.R. Joshi, O. Vozniuk, A. Grünert, C. Ochoa-Hernández, H. Jabraoui, M. Badawi, W. Schmidt, Proton Mobility, Intrinsic Acid Strength, and Acid Site Location in Zeolites Revealed by Varying Temperature Infrared Spectroscopy and Density Functional Theory Studies, J. Am. Chem. Soc. 140 (2018) 17790–17799. https://doi.org/10.1021/jacs.8b11588.
[43] R. E. Fletcher, S. Ling, B. Slater, Violations of Löwenstein's rule in zeolites, Chemical Science. 8 (2017) 7483–7491. https://doi.org/10.1039/C7SC02531A.